Skewed Rotation Symmetry Group Detection

Seungkyu Lee, *Student Member, IEEE,* and Yanxi Liu, *Senior Member, IEEE*

Abstract—We present a novel and effective algorithm for affinely skewed rotation symmetry group detection from real-world images. We define a complete skewed rotation symmetry detection problem as discovering five independent properties of a skewed rotation symmetry group: (1) the center of rotation; (2) the affine deformation; (3) the type of the symmetry group; (4) the cardinality of the symmetry group; and (5) the supporting region of the symmetry group in the image. We propose a frieze-expansion (FE) method that transforms rotation symmetry group detection into a simple, one dimensional translation symmetry detection problem. We define and construct a pair of rotational symmetry saliency maps, complemented by a local feature method. Frequency analysis, using Discrete Fourier Transform (DFT), is applied to the Frieze-expansion patterns (FEPs) to uncover the types (cyclic, dihedral and O(2)), the cardinalities and the corresponding supporting regions, concentric or otherwise, of multiple rotation symmetry groups in an image. The phase information of the FEP is used to rectify affinely skewed rotation symmetry groups. Our result advances the state of the art in symmetry detection by offering a unique combination of region-based, feature-based and frequency-based approaches. Experimental results on 170 synthetic and natural images demonstrate superior performance of our rotation symmetry detection algorithm over existing methods.

Index Terms—Skewed rotation symmetry, Symmetry group, Frieze expansion, Discrete Fourier Transform, Saliency map.

1 Introduction

Symmetry is omnipresent in nature and the man-made world. Symmetric structures stand out from a complex background and attract human attention in natural scenes [1] [2] [3] [4]. Symmetry detection thus plays an important role in human and animal perception of the real world [5] [6]. Likewise symmetry can and should play an important role for object recognition and classification in computer vision [7] [8]. An efficient and robust symmetry detection algorithm for real world images can benefit many computer vision and graphics applications [9] [10] [11] [12]. A symmetric object can be characterized effectively by its symmetry groups [13], yielding a lower dimensional representation space for object recognition [14], matching [15], segmentation [16] and tracking [17].

Rotation symmetry is one of the four mathematically well-defined 2D primitive symmetry types [13]. Many objects such as flowers, hats, lamp shades, dinner plates, bicycle and car wheels demonstrate distinct rotation symmetry patterns (Figures 2, 5, 7, 8, 9, 12, 13, 14, 15, 17, 19). There are three types of Euclidean rotation symmetry groups for 2D objects, namely the cyclic (C_n), the dihedral (D_n) and the symmetry group of a disk $O(2)$ (Figure 1). Any detected 2D rotation symmetry group can be classified as one of these three symmetry groups. Figure 1 demonstrates examples of all three distinct types of rotation symmetry groups about a fixed point in 2D Euclidean space before and after an affine skewing.

- *Seungkyu Lee, Department of Computer Science and Engineering, Pennsylvania State University, University Park, PA 16802. E-mail: sklee@psu.edu*
- *Dr. Yanxi Liu, Departments of Computer Science and Engineering and Electrical Engineering, Pennsylvania State University, University Park, PA 16802. E-mail: yanxi@cse.psu.edu.*

Even though the appearance of real world rotation symmetry is commonplace, computational methods for automatic rotation symmetry detection are scarce in the literature. In this paper, we focus on a complete characterization of the *affinely-skewed rotation symmetry group* of an object in an image as the detection of the following (Figure 1):

1) center of the rotation symmetry,
2) affine deformation (Orientation & Aspect ratio),
3) type of the symmetry group (Cyclic/Dihedral/O(2)),
4) cardinality of the symmetry group (number of folds), and
5) supporting regions for the symmetry group (annulus).

Given a real image, our algorithm detects these five properties of a skewed rotation symmetry group in two steps, *Stage 1* for rotation center and affine rectification detection (properties #1 and #2) and *Stage 2* for symmetry group type, order and supporting region analysis (properties #3, #4 and #5) (Figure 2).

The main contribution of our work includes: (1) The first complete skewed rotation symmetry group characterization: Our algorithm detects and discriminates all three types of rotation symmetry groups and all five properties of a rotation symmetry group (Figure 1) up to an affine transformation. (2) A novel Frieze-expansion (FE) method, which converts 2D rotation symmetry detection into a 1D translation symmetry detection problem and facilitates the affine rectification of the input image using phase information. (3) A pair of novel point-wise rotation symmetry strength (RSS) and symmetry shape density (SSD) saliency maps that can be used to recursively detect potential centers of rotation symmetry, incorporated with a local feature detection method. (4)

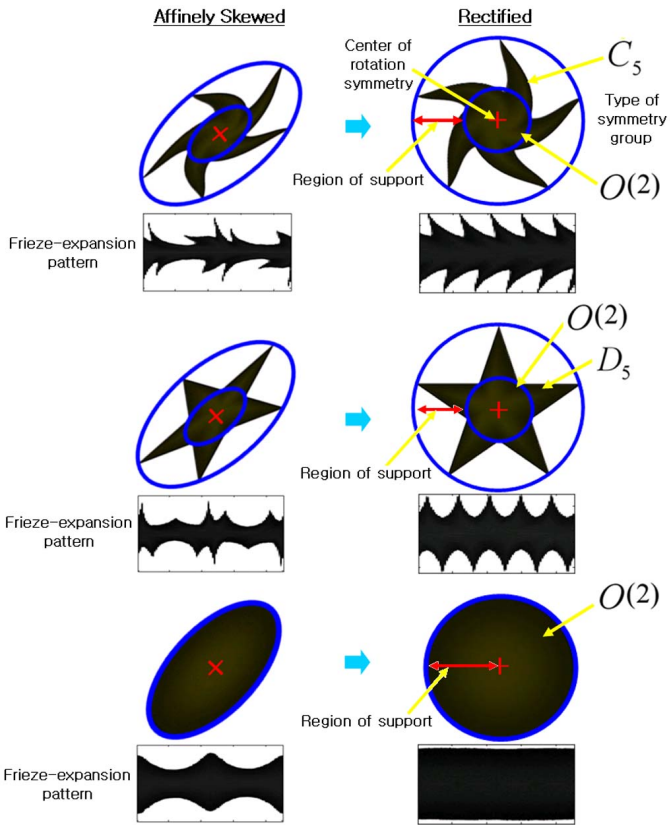

Fig. 1. There are only three different types of rotation symmetry groups of finite shapes in 2D Euclidean space. Left column: affine-skewed symmetry. Right column: affine-rectified (Euclidean) symmetry. C_n: n-fold cyclic group (rotation symmetry only). D_n: n-fold dihedral group (rotation + reflection symmetry) that contains a cyclic subgroup (C_n). $O(2)$: Continuous rotation with infinite number of reflection symmetries about the axes through the center of the circle. The red arrows indicate the annulus region supporting the rotation symmetry

A quantitative evaluation scheme containing both a set of diverse test images under various viewing conditions and labeled ground truth. (5) A comprehensive set of quantitative comparisons against state of the art rotation symmetry detection algorithms, which sets a benchmark for future rotation symmetry algorithms.

2 Related Work

Automatic symmetry detection has been a topic of interest for as long as computer vision has been in existence, though the primary interest had been on the detection of reflection symmetries [7], [18]–[22]. We focus our assessment on rotation symmetry detection algorithms from real images. There are mainly two different approaches: local feature-based methods that detect symmetries from a set of selected key points, and global region-based methods that detect symmetries using all pixels of an image.

Local feature-based algorithms have the advantage of being more efficient for rotation symmetry detection. Reisfeld et. al. [4] propose a specific rotation symmetry saliency map computed from a pair of perpendicular point-wise reflection symmetries, thus favoring objects in the dihedral symmetry group D_4 only. Zabrodsky et.al. [18] introduce a concept of continuous symmetry of a shape by computing the minimum mean squared distance between the contour points of an object in an image and its symmetrical shape. In 2005, Prasad and Davis [23] proposed a novel Gradient Vector Flow (GVF) method, using a confidence map to detect the candidate rotation symmetry centers from real images. This work, though only tested on images of flowers, is a significant step forward in rotation symmetry detection where the algorithm is applied directly to un-segmented, real world images with multiple symmetries. However, [23] requires the number of the fold (number of repetition in angular direction) to be given. It takes several minutes to several hours to process a single image due to its super-linear algorithm complexity in the number of corresponding locations and the number of pixels. Also in 2005, Liu et. al. [24] proposed a dihedral and frieze group detection algorithm for photos of papercut patterns using edge features (code is publicly available at http://vision.cse.psu.edu/papercut.htm). Their algorithm searches through the whole 2D polar parameter space of reflection axes and uses the structure of the found reflection axes to detect dihedral and frieze groups. In 2006, Loy and Eklundh [25] proposed a pairwise local feature matching algorithm using SIFT key points at corresponding locations. This method is considered to be one of the best (and fastest) symmetry detection algorithms based on a recent quantitative evaluation of discrete symmetry detection algorithms [7]. Their algorithm detects rotation symmetry centers and number of folds from real images, but does not address all five symmetry group properties. A quantitative comparison of our proposed method with [25] is provided in Tables 1-3.

Global region-based methods, on the other hand, provide a more complete characterization of all potential symmetries in the image. Derrode and Ghorbel [26] introduce the Fourier-Mellin transform for rotation symmetry detection but the algorithm requires that an input image has a single rotation center and a clean background. Keller and Shkolnisky [27] introduce a global geometric structure method that is the closest to our proposed method, using pseudo-polar Fourier transform to find repetition over angular direction for rotation symmetry detection. However, the algorithm is limited to detecting a single non-skewed rotation symmetry at a time in each image. Our earlier work on rotation symmetry detection [28] using Frieze-expansion (FE) and frequency analysis is a region-based method, calculating a Rotation Symmetry Strength (RSS) map for all pixels in an image. It is limited to finding non-affinely skewed rotation symmetries only.

In addition to the Euclidean symmetry detection algorithms, there is a large body of work on skewed-reflection symmetry detection [19]–[22]. Kanade intro-

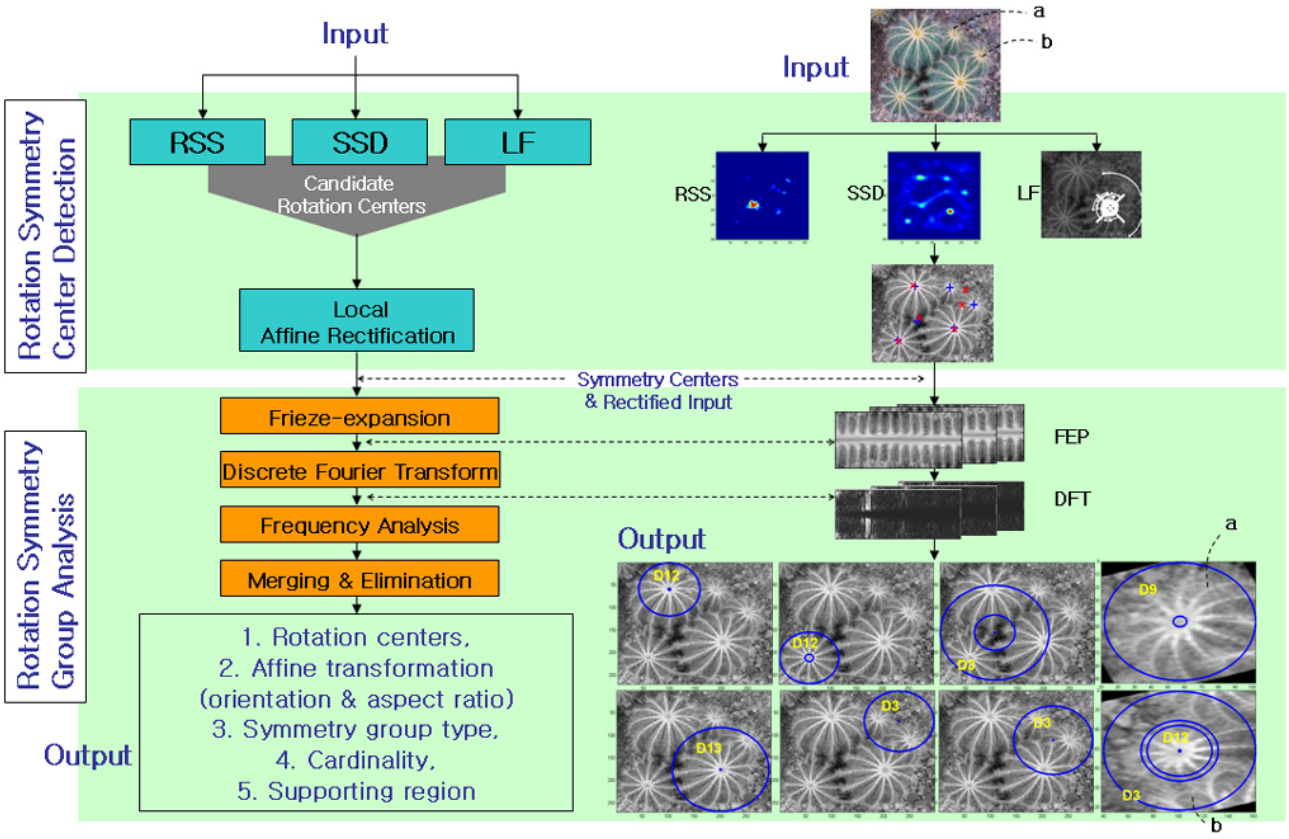

Fig. 2. Flowchart of our proposed algorithm: It consists of two main stages; (1) center detection and (2) symmetry group analysis (See Fig 4 for more details). RSS: Rotation Symmetry Strength (Section 3.2.1), SSD: Symmetry Shape Density (Section 3.2.3), LF=Local Features, FEP=Frieze Expansion Pattern, DFT=Discrete Fourier Transform.

duced the term *skewed symmetry* [19] denoting globally affine or perspective skewed reflection symmetry. Van Gool et al. [22] deal with skewed point symmetry (2-fold rotation) by detecting the reflection symmetries of pairs of pixels from a potential rotation center. The rotation symmetry detection algorithms developed by Yip et al. [29], Lei and Wong [30] and Shen et al. [31] share the same goal of finding the dihedral rotation symmetry groups only (Figure 1), and they require an object being placed on a clean background. There is relatively little literature on effective skewed *rotation symmetry* detection directly from real images. Cornelius and Loy propose an affine-transformed version [32] [1] of Loy and Eklundh's rotation symmetry detection algorithm [25] that performs an exhaustive search through all discretized orientation and tilt angles (850 iterations). Carlsson [33] provides a general mathematical characterization of rotational symmetry in perspective space. Though the formulation is general, the method requires a sufficient number of parallel lines on the object for vanishing point detection, posing difficulties in applying the theory to general real objects (see Figures 12-17).

To the best of our knowledge, none of the existing rotation symmetry detection algorithms [22]–[28], [30]–[33] have attempted to characterize the five properties (the center, deformation, type, cardinality and supporting region of the detected rotation symmetry group) of affinely skewed rotation symmetry groups from unsegmented real images simultaneously and automatically, as we propose to do in this work.

1. Up to the publication of this paper, we are unable to obtain the original code or executable of [32] for a fair comparison study.

3 Our Approach

The existence of a rotational symmetry in an image is usually supported by an annulus containing a repeated pattern along its angular direction (Figure 1). A key observation in our work is that the angularly repeated pattern (rotation symmetry) can be detected and analyzed more efficiently in a polar space as a linearly repeated pattern (translation symmetry). Our approach exploits the interplay between discrete rotation symmetry groups in a Cartesian space and the frieze translation symmetry groups in the corresponding polar space (Figure 3). Figure 2 provides an overview of our proposed rotation symmetry detection approach. Each component of our approach is explained in detail below.

3.1 Frieze-Expansion

Given a potential rotation center (x, y) in an image and an angular step size $2\pi/N$, we propose a **Frieze-expansion (FE)** process to rotate each diameter (starting

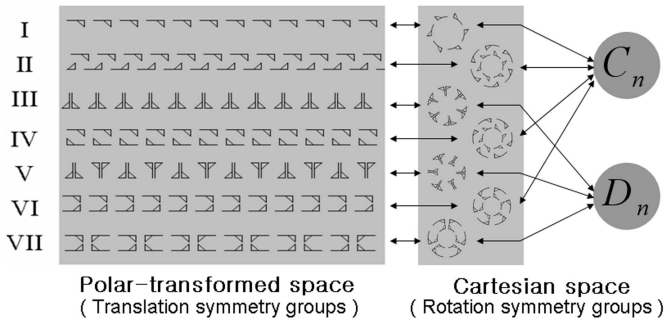

Fig. 3. There is a unique correspondence between the seven frieze groups in the frieze-expansion patterns and the two discrete rotation symmetry groups in 2D Cartesian space.

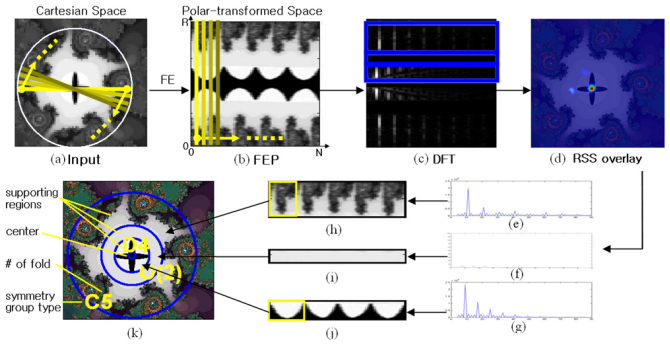

Fig. 4. (a) Original image; a point (x,y) is selected as a potential symmetry center. (b) Frieze-expansion (FE) [28] transforms a rotation symmetry in Cartesian space to a Frieze-expansion pattern (FEP) with translation symmetries in a polar-transformed space. N is the width of the FEP which is the resolution of the FE. R is the height of the FEP and corresponds to the diameter of the largest possible circular region (centered at (x,y))contained within the input image. (c) 1D DFT of the FEP (row-by-row); horizontal axis is the index of DFT basis and segmented regions are marked in blue lines. (d) RSS overlaid on the original image. (e)(f)(g) are the sum of absolute DFT coefficients of the segmented regions in (c) respectively. (h)(i)(j) are the segmented frieze patterns from (b). (k) Final rotation symmetry group detection result.

from the horizontal diameter) going through (x, y) to its vertical position and to re-align them consecutively from left to right while advancing about the center (x, y) clockwise in the original image (Figure 4 (a),(b)). The obtained pattern is called a **Frieze-expansion pattern (FEP)**(Figure 4 (b)). If the candidate center location (x, y) in the original image is indeed the center of a rotational symmetry, the FEP becomes a true frieze pattern [34] with non-trivial horizontal translation symmetry. Since dihedral and cyclic groups are the only discrete rotation symmetry groups and O(2) is the only continuous symmetry group of a 2D object (Figure 1), there exists a unique, mathematically proven, bijective relation between the discrete rotation symmetry groups $(C_n, D_n, O(2))$ and the seven frieze groups [13] (Figure 3). If there is a rotation symmetry in an image, the symmetry group of its FEP must fall into one of the seven frieze groups. Figure 3 shows the correspondence of the seven frieze groups and two discrete rotational symmetry groups under their respective spaces. A constant FEP corresponds to a continuous rotation symmetry group $O(2)$. Instead of finding rotation symmetry properties of an object in its original space, we propose to detect its corresponding translation symmetry of FEP and treat symmetry group O(2) as a special case of FEPs. We only use the upper half of FEP for rotation symmetry detection given the redundancy of the upper and lower halves of FEP (in Figure 4 (b)). However, we do keep the full (the upper and lower halves) FEP because it reveals important information about the cardinality, as will be explained in Section 3.4.2.

3.2 Stage 1: Center of Rotation Detection

We propose a rotation center detection method that combines a set of rotation symmetry saliency maps from (1) a pointwise Rotation Symmetry-Strength (RSS) measure computed from the DFT coefficients of FEP, (2) a Symmetry Shape Density (SSD) function defined in terms of the phase information of FEP, and (3) a potential rotation center map based on local feature matchings. Potential rotation centers are detected by finding local peaks of RSS and SSD saliency maps combined with the probable rotation centers from pairwise local feature matching. All centers from these three different rotation symmetry saliency maps are collectively considered as potential rotation centers.

3.2.1 Rotation Symmetry Strength (RSS)

Let $p_{x,y}(r, n)$ be an $N \times R$ FEP (Figure 4 (b)) expanded at an image position (x, y) where r∈[1,R], n∈[1,N], R and N are the height and width of the FEP respectively. A one-dimensional horizontal discrete Fourier transform (DFT) is performed on each row of the FEP. The k^{th} coefficient of the DFT [35] of the r^{th} row, $P_{x,y}(r, k)$ is

$$P_{x,y}(r,k) = a_{x,y}(r,k) + ib_{x,y}(r,k)$$
$$= \sum_{n=1}^{N} p_{x,y}(r,n) e^{-i\frac{2\pi}{N}(n-1)(k-1)} \quad (1)$$

where $a_{x,y}(r, k)$ is the real part and $b_{x,y}(r, k)$ is the imaginary part of the DFT coefficient. $P_{x,y}(r, k)$ represents the complex value of each frequency component of the spatial domain information $p_{x,y}(r, n)$.

$S_{x,y}(r, k)$ is the energy spectral density of $p_{x,y}(r, n)$:

$$S_{x,y}(r,k) = \overline{P_{x,y}(r,k)} P_{x,y}(r,k) = a_{x,y}(r,k)^2 + b_{x,y}(r,k)^2 \quad (2)$$

The value of $S_{x,y}(r, k)$ reflects the relative strength of a translational symmetry with the k^{th} potential frequency. All possible phase differences between $p_{x,y}(r, n)$ and one of the corresponding DFT components (sine or cosine wave) are between 0 and $\frac{\pi}{2}$, which corresponds to the DFT phase. With the angular step size $\frac{2\pi}{N}$, we have N points for each row of the FEP and N coefficients for each

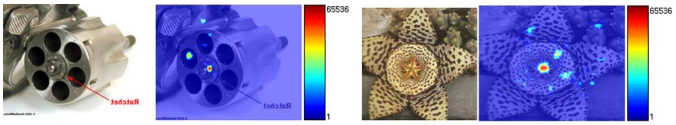

Fig. 5. Sample rotation symmetry saliency (RSS) map overlaid on real images. * Best viewed in color

corresponding spectral density. Due to the symmetric nature of DFT coefficients [35], only the first half ($k = 2...\frac{N}{2}$) of the $S_{x,y}(r,k)$ excluding DC coefficient ($k = 1$) need to be considered.

Originally, Rotation symmetry strength (RSS) is a function of center position (x, y), the radius r and the angular step size θ. In the rotation center detection step of our algorithm, the largest circle with radius r inside the given image for each center location (x, y) is used (Figure 4 (a)) and the angular step size θ is fixed to $\frac{2\pi}{N}$, where $N = 90$ in all our experiments. RSS then becomes a function of position (x, y) only and can be represented as a two dimensional RSS map. Higher values of RSS imply higher likelihood of rotation symmetry centered at that location. By calculating RSS values at each pixel of an image we can construct a pointwise RSS map, which reveals the rotation symmetry saliency of the given image (Figure 5).

Let $k_{peak}(r)$ be the DFT coefficients of the r^{th} row satisfying $S_{x,y}(r, k_{peak}) \geq mean\{S_{x,y}(r,k)|k = 2,3,4,...,\frac{N}{2}\} + 2 \cdot std\{S_{x,y}(r,k)|k = 2,3,4,...,\frac{N}{2}\}$. Rotation symmetry strength (RSS) at an image position (x, y) can then be defined as:

$$RSS(x,y) = \sum_{r=1}^{R} \rho_r \frac{mean(S_{x,y}(r, k_{peak}(r)))}{mean(S_{x,y}(r,k))} \quad (3)$$

where,

$$\rho_r = \begin{cases} 1, & if \quad Mod(k_{peak}(r), min(k_{peak}(r))) = 0 \\ 0, & otherwise \end{cases}$$

In the frequency domain, we need to check the coincidence among $S_{x,y}(r, k_{peak}(r))$ entries to confirm that all indices $k_{peak}(r)$ are multiples of the smallest index. If all $k_{peak}(r)$ indices satisfy this condition, it means that they support the same repeated pattern. Therefore there exists a rotational symmetry in the row (ρ_r=1).

We use a hierarchical search algorithm to accelerate the process. We start from the observation that most rotation symmetries remain when an image is scaled down. We perform a full search over the smallest image level at the top of the image pyramid. The initial RSS map provides the potential centers of rotation symmetries and is enlarged using bilinear interpolation to the size of the next level of the pyramid. RSS of the neighborhood regions of the detected potential center points are refined at a higher resolution. This process repeats until we reach the original image resolution. We select the final candidate symmetry center points at the highest resolution. We adopt a well-known peak visiting method

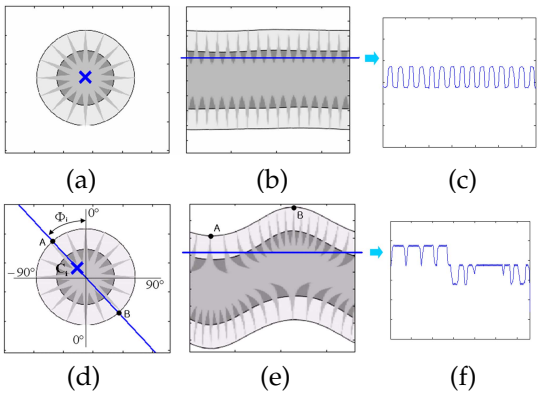

Fig. 6. Bidirectional flow (a) A rotationally symmetric object with a rotation center x. (b) FEP of (a): when expanded around the correct center, its FEP is a true frieze pattern characterized by translation symmetries. (c) Intensity variation example of a single row of (b). (d) A rotation symmetry object with an arbitrary sample point. Indicated angles represent phase of the 2nd DFT component. Flow line (blue) is intersecting the rotation center. (e) FEP of (d): if the center of FE is off (blue x), a single cycle of sine wave component is formed in its FEP. (f) Intensity variation of a single row of (e).

called the inhibition-of-return mechanism [36] to extract local maxima in descending order of the RSS saliency map. We continue to extract local maxima until the RSS value falls below a threshold, $mean(RSS)+\beta\times std(RSS)$.

3.2.2 Bidirectional Flow

To construct a phase-based rotation symmetry saliency map, we propose a bidirectional flow vector. Figure 6(a) is an input image with a detected center (marked with an x) and Figure 6(b) is its FEP at x. With the correct rotation center, its FEP shows horizontal translational symmetry (Frieze pattern), while an off-centered point (Figure 6(d)) leads to a distorted frieze pattern as its FEP (Figure 6(e)). Points A and B in Figure 6(d) (on the boundary with the shortest and the longest distance from the off-centered point, respectively) are also indicated in Figure 6(e). The FEP is distorted by a single cycle wave with an arbitrary phase due to the off-centered point. Intensity variations along each row of the FEP also have a single cycle wave component with the identical phase. Now consider performing a 1-dimensional DFT on each row. The 2nd component of the DFT characterizes the single cycle wave on FEP. Angle Φ in Figure 6(d) corresponds to the phase of the 2nd DFT component in each row of FEP.

Let $c_i = (x_i, y_i)$ be an arbitrary point near the correct rotation symmetry center and $P_{x_i,y_i}(r,k)$ be the DFT coefficients of the r^{th} row of FEP based on c_i. Then $\phi_i(r)$ is defined as the phase of the 2nd DFT component for the r^{th} row:

$$\phi_i(r) = arctan(\frac{Re(P_{x_i,y_i}(r,2))}{Im(P_{x_i,y_i}(r,2))}) \quad (4)$$

Phase of c_i is calculated by taking the median of the phase values $\Phi_i = median(\phi_i(r))$. Now, we can draw a

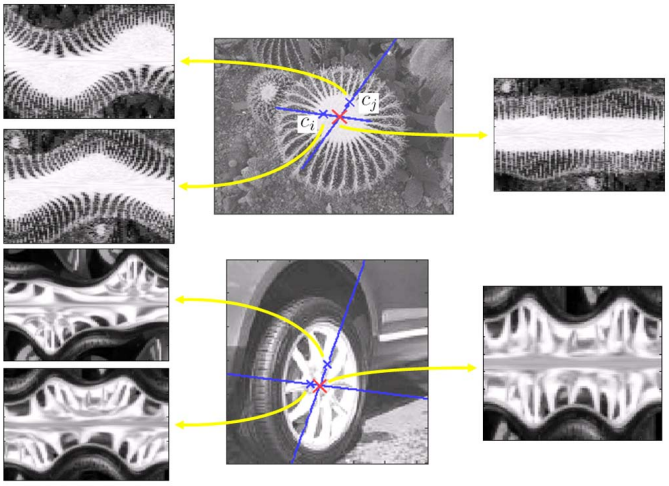

(a) FEPs (b)Input image (c)FEPs of the true centers

Fig. 7. Bidirectional flow examples: (a) Two off-centered FEPs (blue x's shown in (b)). (b) True center (marked with a red x) estimated by intersecting two bidirectional flows obtained from two arbitrary off-centered points (marked with a blue x). (c) New FEP from the estimated true rotation center (red x).

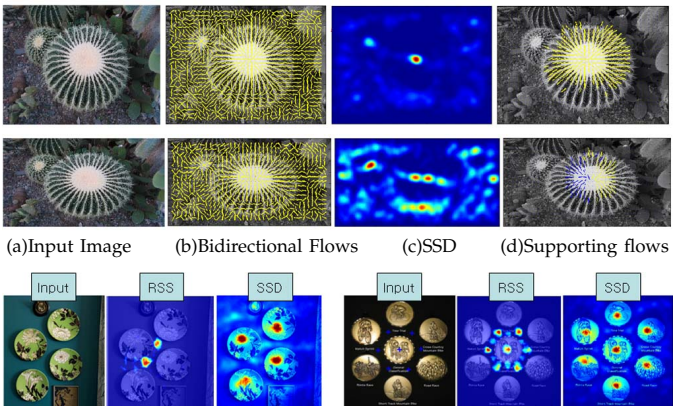

(a)Input Image (b)Bidirectional Flows (c)SSD (d)Supporting flows

RSS and SSD complement each other in rotation symmetry center detection

Fig. 8. Symmetrical Shape Density (SSD) maps and bidirectional flows overlaid on real images. Middle row is the affine-skewed version of the top row. (b) Bidirectional flows from the discretized image locations (c) All intersecting points of those pairs build the SSD after smoothing with a Gaussian kernel (d) Supporting flows for high density points. A single mode of SSD is supported by points from all circular directions. Affinely skewed object has a pair of modes: blue flows for the left mode and yellow flows for the right mode. Bottom row: complementary RSS (between objects) and SSD (on an object) for rotation symmetry center detection.

line through the point c_i with slope($-\frac{1}{tan\Phi_i}$) calculated from its phase. We define this line as a *bidirectional flow* of the point c_i. The potential correct rotation center should lie on the bidirectional flow because the bidirectional flow points to the shortest(A) and the longest(B) locations from c_i (Figure 6(c)). The bidirectional flow line is defined as:

$$\frac{tan\Phi_i}{x_i + y_i tan\Phi_i} y + \frac{1}{x_i + y_i tan\Phi_i} x = 1 \qquad (5)$$

If we have another point $c_j = (x_j, y_j)$ that is not on the bidirectional flow of c_i, we can estimate the potential rotation symmetry center C by intersecting the two bidirectional flows detected separately through phase analysis:

$$C = \begin{pmatrix} x \\ y \end{pmatrix} = \begin{pmatrix} \frac{s_i x_i - s_j x_j + y_j - y_i}{s_i - s_j} \\ \frac{s_i s_j (x_i - x_j) + s_i y_j - s_j y_i}{s_i - s_j} \end{pmatrix} \qquad (6)$$

where $s_i = -\frac{1}{tan\Phi_i}$ and $s_j = -\frac{1}{tan\Phi_j}$ are slopes of the intersecting lines respectively (see the examples in Figure 7).

Figure 6(d) shows the phase Φ_i along the location of an off-centered point. If the sample point is located at the left(right) half circle, the phase is negative(positive). Note that the phase angle is discretized by the step size of FE. Therefore, there exists a maximum phase estimation error of $e_{max} = \left(\frac{180}{N}\right)^o$ where N is the number of columns of FEP. We compute all bidirectional flows from discretely sampled points of a given image, shown as short oriented line segments centered on the sample points (Figure 8 (b)).

3.2.3 Symmetry Shape Density (SSD)

Each pair of bidirectional flows has one intersecting point, which indicates a potential rotation symmetry center. With a set of z bidirectional flows we can calculate at most $\frac{z^2-z}{2}$ intersecting points. We define ***Symmetry Shape Density*** $SSD(x, y)$ as the convolution of the intersecting point distribution $D(x, y)$ with a $l \times l$ Gaussian kernel $G(l, l)$ ($SSD(x, y) = D(x, y) \bullet G(l, l)$), where l and the sigma of the Gaussian kernel are proportional to the image size. Each value of $D(x, y)$ corresponds to the cumulative number of intersecting points C at the location (x, y) calculated in the equation (6).

Figure 8 (b) is an example of a bidirectional flow map and Figure 8 (c) is its SSD. The true rotation center points have higher symmetry shape density. By using the same peak visiting method called the inhibition-of-return mechanism [36], we can measure the potential rotation symmetries at each image location. Figure 8 (bottom row) shows how RSS and SSD work complementarily in detecting different types (between objects vs on an object) of rotation symmetries.

With an affinely transformed symmetry, there are two high-density points located on the major axis of the elliptical shape of the symmetric object (Figure 8 (d)). This characteristic enables us to locate the center of an affinely transformed object by taking the middle point of the two high-density points and the orientation of the affine transformation by taking the orientation of the major axis recovered by connecting the two high-density points. The remaining problem is how to decide whether a high-density point is a single point of a non-affine transformed object or one of the two points of an affinely transformed object. Figure 8 shows the two different types of high-density points (from affine and non-affine objects). Yellow and blue lines of Figure 8 (d) represent the bidirectional flows contributing to the high

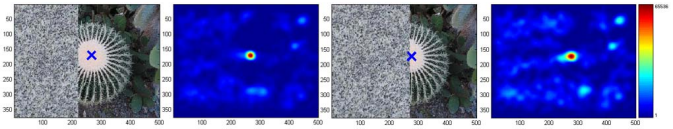

Fig. 9. SSD map and detected centers under occlusion

density of the SSD. One of the high-density points of the affinely transformed object is supported by sample points from one-half circle (blue) and there is another center point in the pair supported by sample points from the other half circle (yellow). By storing the pattern of the supporting sample points (half ellipse or full circle) for each intersecting point, we can decide whether a high-density point comes from an affinely transformed object or not. Figure 9 is an example showing the potential for rotation symmetry center detection using SSD on occluded images.

3.2.4 Rotation Symmetry Center Localization

In addition to the two different types of rotation symmetry saliency maps (RSS and SSD), we also incorporate a rotation symmetry center detection method using local features (LF). Similar to [25], we use the potential centers of rotation symmetry from feature matching. Our experiments include, but are not limited to, SIFT key features. We collect all centers from the three rotation symmetry saliency maps (RSS, SSD and LF) as the potential centers of rotation symmetries.

3.3 Stage 1: Affine Deformation Estimation

Real world images taken from an arbitrary angle often contain perspective distortion caused by the projection of a 3D object into a 2D planar space. In most cases, however, objects are of limited spatial extent and far enough away from the focal point of a camera so that we can use a weak perspective approximation [30]. Therefore, affine transformation estimation of rotation symmetry in real world images has a justifiably wide applicability in computer vision.

After the construction of a set of rotation symmetry saliency maps, we perform a phase analysis on the FEP to estimate potential affine transformations. We then analyze the symmetry group on the rectified image. We re-calculate new rotation symmetry strength values after rectification on each potential center. The orientation and skew components are the two unknown variables for affine rectification, corresponding to an estimation of (1)the amount of rotation from the zero-phase axis and (2)the aspect ratio, respectively.

The orientation can be predicted by drawing the major axis of an ellipse intersecting the pair of high density points found in the SSD map. In this section, we detect the orientation using low frequency phase analysis. Figure 10 (a) shows an affinely transformed image of Figure 6 (a) and Figure 10 (b) is its FEP. We can observe a sine wave pattern repeated twice in Figure 10 (b). This

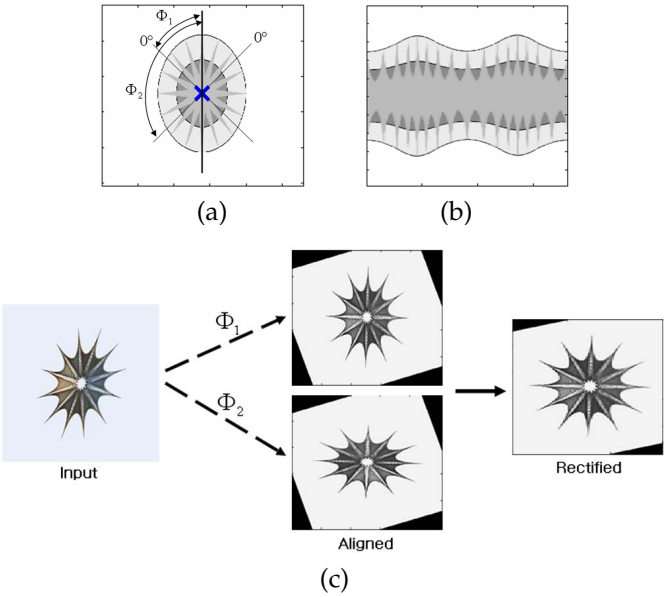

Fig. 10. (a) Affinely transformed rotation symmetry object with true center. (b) FEP of (a): if the center is correct, only sine wave of double cycles formed in its FEP (c) Orientation detection and alignment for both phase values (Φ_1 and Φ_2) defined in Equation (16).

means that the intensity variations along each row of the FEP repeat twice with identical phase. Now we perform a 1-dimensional DFT on each row and investigate the 3rd DFT component, which corresponds to the double repetition (k_{th} DFT component correspondes to the $k-1$ repetition). The phase of the 3rd component corresponds to $\Phi_1 = median(\Phi(r))$ in Figure 10 (a), where

$$\Phi(r) = arctan(\frac{Re(P_{x,y}(r,3))}{Im(P_{x,y}(r,3))}). \quad (7)$$

The phase could be detected and aligned to either the object or the background because the algorithm does not know which region is from the object. Therefore, in this step, we have an additional possible orientation of phase $\Phi_2 = \Phi_1 + \frac{2}{\pi}$. Figure 10 (a) shows the phase angle for both the long and short axes of the object. Two zero-phase axes from both object and background are shown. Figure 10 (c) shows the orientation detection and alignment results for both phase values. Note that if we have affinely skewed rotation symmetry, we can easily estimate the orientation from the two high density point pairs detected by SSD. Then, we can decide and verify the correct orientation by choosing the phase with the closer to this estimated orientation. If there is no estimated orientation from the previous step, both cases should be investigated.

The long axis of an affinely transformed symmetry is aligned to either the horizontal or vertical axis (Figure 10) for both phases. We calculate and compare RSS values for each different aspect ratio of the aligned images by changing the length of the x-axis. In other words, we calculate RSS values for all ratio steps between 1:1 and 1:$\sigma(0 < \sigma < 1)$. The aspect ratio that maximizes

RSS is selected. In our experiments, $\sigma = 0.5$ and the step size is 0.05. Equation (8) shows the inverse affine transformation matrix of a given image:

$$T = \begin{bmatrix} \alpha & 0 \\ 0 & 1 \end{bmatrix} \begin{bmatrix} cos(\frac{\hat{\Phi}-90}{2}) & -sin(\frac{\hat{\Phi}-90}{2}) \\ sin(\frac{\hat{\Phi}-90}{2}) & cos(\frac{\hat{\Phi}-90}{2}) \end{bmatrix} = \begin{bmatrix} \alpha cos(\frac{\hat{\Phi}-90}{2}) & -\alpha sin(\frac{\hat{\Phi}-90}{2}) \\ sin(\frac{\hat{\Phi}-90}{2}) & cos(\frac{\hat{\Phi}-90}{2}) \end{bmatrix} \quad (8)$$

where $\alpha(\sigma \leq \alpha \leq 1)$ is the aspect ratio and $\hat{\Phi}$ is the phase of the maximum RSS. Transformation T maps a given affinely transformed planar symmetric object to its maximum Euclidean symmetry, upon which we perform a frequency analysis to find its rectified rotation symmetry group. Each potential center can have a different affine transformation that will be detected and rectified separately. Based on the rectified rotation symmetry image, we calculate RSS values of the potential rotation symmetry centers and perform peak visiting again to eliminate further potential rotation symmetry centers below the threshold. Since originally elliptical objects (R42 of Figure 19) have an inherent ambiguity from a single view, our algorithm always finds the implied circular rotation symmetry object by an affine rectification.

3.4 Stage 2: Symmetry Group Analysis

With the affine rectified image, we are now ready to investigate the cardinality (fold), rotation symmetry group type (Dihedral/Cyclic/O(2)) and corresponding supporting regions of detected rotation symmetry groups [28]. Figure 4 illustrates how symmetry groups can be analyzed using the spectral density. The number of folds corresponds to $k-1$ when the k_{th} DFT component has the highest coefficient. The symmetry supporting region can be obtained by segmenting consecutive rows of the FEP with similarly high coefficient in the spectral density plot (Figure 4 (b)). Finally, to classify symmetry group types, we use the proven relationship between translation symmetry group (frieze groups) and the 2D rotation symmetry groups (Figure 3). The key to distinguish between Dihedral and Cyclic groups is whether the FEP has a vertical reflection symmetry.

3.4.1 Supporting Region Segmentation

As can be seen in Figure 4(c), several consecutive rows may have similar peak distributions of the DFT spectral density. This indicates a "frequency cluster" leading to one contiguous symmetry-supporting region. We can therefore differentiate one symmetry region from another type of symmetry region (circular bands) even though they share the same center. By grouping consecutive dominant peaks, we can delineate each symmetry region on both the converted frieze pattern and the original image. With real world images, noise can cause detection failure in a narrow band and divide one

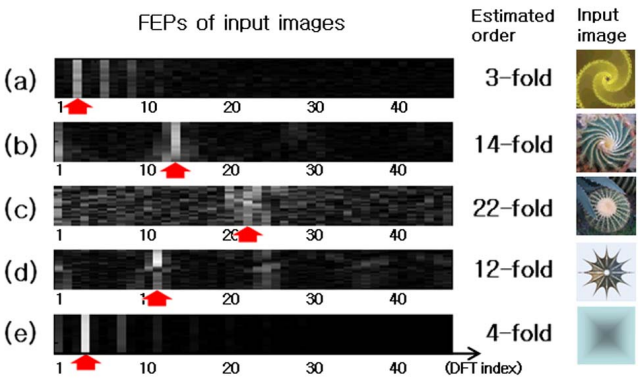

Fig. 11. Examples of determining the number of folds from segmented FEPs. Red arrows indicate the dominant coefficient, each of which corresponds to (a) 4th , (b) 15th , (c) 23th , (d) 13th and (f) 5th DFT coefficient. The fold is $DFTcoefficient-1$ (Section 3.4).

symmetry region into multiple subregions, even though they have the same symmetry characteristics. To avoid this problem, we merge consecutive symmetry bands if they share the same number of folds and symmetry type. Similarly, we eliminate narrow symmetry regions that are hardly perceived by the human eye. Figure 4(c) shows a segmented result. Figure 4(e) shows the summed DFT power spectrum of corresponding symmetry regions, from which we can decide the number of folds.

3.4.2 Estimating Symmetry Group Cardinality

From the DFT coefficient plot of each supporting region, we find the highest coefficient basis k. The number of folds corresponds to k-1. Note that we only consider AC coefficients. For example, the 7th coefficient is associated with the cosine/sine waves with six cycles [39]. This responds most strongly to the six-fold rotation symmetry. In Figure 4, the summed up DFT density plot in (e) has a maximum peak at the 6th component and (g) has its maximum peak at the 5th component, which represents a 5-fold and a 4-fold rotation symmetry, respectively. The reader can verify this with respect to the corresponding frieze patterns in Figure 4(h) and (j). Figure 11 shows several fold decision examples from the DFT spectral density image. If a Frieze expansion has horizontal reflection symmetry with respect to the center row (Figure 4(b)), the inverse Frieze expansion in its image space has a rotation symmetry with even fold, otherwise it is odd. For example, the pattern in Figure 4(j) is reflected symmetrically in figure 4(b), but the pattern in 4(h) is not. This knowledge helps to decide the number of folds robustly.

3.4.3 Symmetry Group Classification

We can prove that a FEP of cyclic symmetry has no vertical reflection, while a FEP of dihedral symmetry has to have vertical reflection (Figure 3). By checking the existence of vertical reflection in a frieze pattern, we

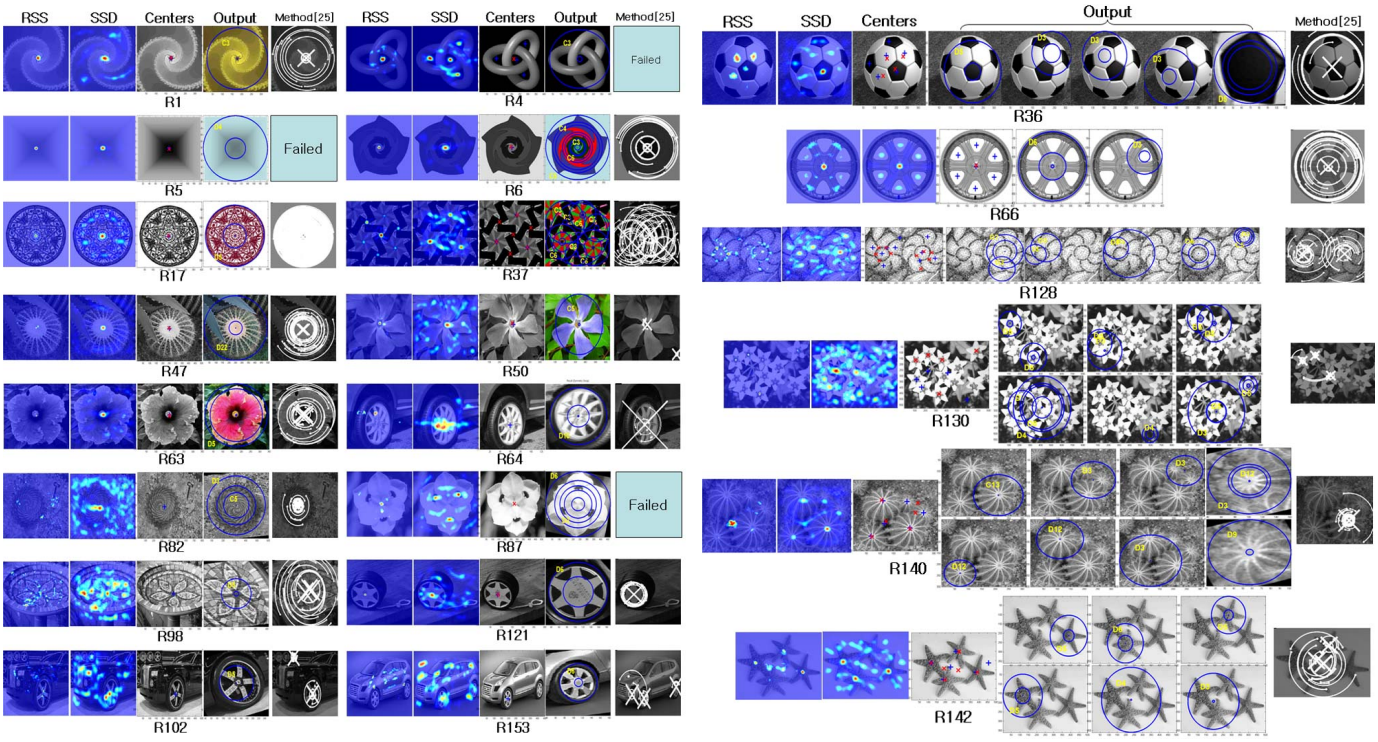

Fig. 12. Sample experimental results with synthetic and real images for all five rotation symmetry properties (center, type, # of folds, supporting region and affine transformation). R98 and R121 are from Caltech-256 [37], R102 is from PASCAL [38]. Supporting region of affinely skewed objects are shown in rectified image. * Best viewed in color. Red/Blue points are the potential rotation centers found from the RSS and SSD saliency maps (Section 3.2.1 and 3.2.3) respectively. Results of [25] on the same images are shown on the rightmost column.

can differentiate cyclic from dihedral symmetry groups (Figure 3). Furthermore with the fold information, we can identify the tile of a Frieze pattern [34] computationally. We flip a tile (the smallest cell of a frieze pattern) horizontally and slide it over the FEP while calculating correlation. If there is a periodic match corresponding to the dominant frequency we detected from the DFT coefficients investigation, we conclude this region is dihedral, and if not, we conclude that it is cyclic. In other words, if there is vertical reflection in the Frieze pattern, it falls into the dihedral rotation symmetry group. One exception is shown in Figure 4(f). Most of the coefficients are zero, signifying that the corresponding region of the original image is uniform, as in Figure 4(i). This indicates the existence of the continuous rotation symmetry group, O(2).

4 Experimental Results

We evaluate our proposed skewed rotation symmetry group detection algorithm under various conditions using a diverse set of test images. A total of 170 images is collected from the internet and public image data sets like PASCAL [38] and Caltech-256 [37]. Images are categorized into three subsets: 39 synthetic images with both single and multiple rotation symmetries within the same image, 104 real images with a single rotation center and 47 with multiple rotation centers (see supplemental material). We further divide the data set into three ground truth levels for quantitative evaluations. We test two different versions of center detection methods proposed in our approach. Method #1 detects rotation symmetry centers by combining RSS and SSD only and Method #2 incorporates the local feature detection method with Method #1. We use the empirical value $\beta = 1.8$ for the threshold of both saliency maps, $l = (X + Y)/24$ and $sigma = l/4$ for the Gaussian kernel in SSD construction when the image size is $X \times Y$ (see Section 4.1 and Figure 16 for a discussion of the parameter β and detection accuracy).

Figure 12 shows successful results from each of the three test sets respectively. R4 in Figure 12, displays a cyclic 3-fold rotation symmetry with a global center (red) as well as three locally distorted 3-fold symmetry centers (blue). R6 in Figure 12 has multiple co-centered symmetry groups. Supporting regions of the four different cyclic symmetry groups (C3, C6, C4 and C5) are correctly segmented and the symmetry group types are detected. R36 in Figure 12 is a good example demonstrating the multiple symmetry detection performance. Affinely transformed five fold symmetries and three fold symmetries at the centers of hexagons are all found successfully. In the wallpaper patterns like R37 (Figure 12), all symmetry centers are correctly found. These

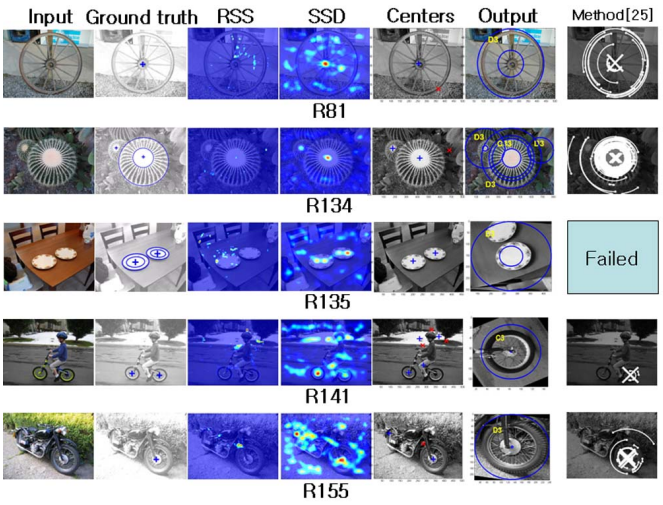

Fig. 13. Center detection success but # of folds or rotation symmetry group type detection failure cases. R141 and R155 are from PASCAL [38]. Results of [25] on the same images are shown on the rightmost column. * Best viewed in color

(a) Level-1 symmetry (global: among objects) (b) Level-2 symmetry (an object) (c) Level-3 symmetry (local: part of an object)

Fig. 14. Three levels of symmetries (among objects, on an object and within an object): Our experiments are evaluated on each level (Table 1-4) respectively.

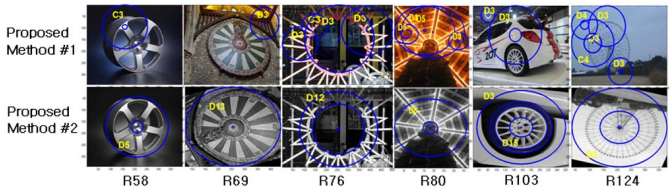

Fig. 15. Rotation symmetry center detection (Table 4): Proposed Method #2 success results where Proposed Method #1 failed. * Best viewed in color. Red/Blue points are the potential rotation centers found from the RSS and SSD maps respectively.

results show the potential ability of lattice (translation symmetry) detection of the proposed algorithm.

R128 (Figure 12) is a good example showing how two symmetry saliency maps (RSS and SSD) complement each other for different types of rotation symmetries. Red/Blue points are the potential rotation centers found by the RSS and SSD respectively. The RSS responds well to the patterned symmetries while the SSD responds well to circular shaped symmetries. R140 in Figure 12 also shows the complementary performance of RSS and SSD. Two cacti on the upper right corner are correctly found although they are small and affinely transformed.

Our proposed algorithm can detect high order of folds (22-fold in R47 in Figure 12 and 33-fold in R134 in Figure 13), occluded objects (R47 in Figure 12) and affinely skewed symmetries (R135 in Figure 13). Figure 13 shows some failure cases (the # of folds or rotation symmetry group type) due to deviation of the center detection, ambiguous cardinality and background clutter.

4.1 Quantitative Evaluation

To evaluate and compare different rotation symmetry detection algorithms on different types of images in a more precise and semantically meaningful (to human) manner, we define three levels of rotation symmetries: (1) rotation symmetry formed by a set of objects (level-1, among objects, Figure 14(a)); (2) rotation symmetry of a single object (level-2, single object, Figure 14(b)); and (3) rotation symmetry of a sub-part of an object (level-3, within one object, Figure 14(c)). This division depends on our definition of an *object*, which is subjective. Here we use the most commonly accepted and least ambiguous concept of everyday object as a basis (from 5 raters). The full test-image sets and their respective labeled ground truth are provided in the supplemental material. Figure 14 shows samples of each image and the corresponding ground truth evaluated.

Tables 1, 2 and 3 summarize the quantitative evaluation and comparison results among [25], [28] and our two proposed rotation symmetry group detection algorithms on the level-1, level-2 and level-3 test image sets, respectively. The Proposed Method #1 using both RSS and SSD shows an overall higher detection rate in all types (Table 1, 2 and 3) than [28] and [25]. The Proposed Method #2 integrating the local feature method with the RSS and the SSD has the best performance rates of all.

Figure 15 shows several challenging cases where the local feature method provides a synergy in the center detection step. Table 4 shows not only the relative difference between a pair of rotation symmetry detection algorithms but also whether the difference is statistically significant in terms of the p-values calculated using paired t-test on each pair of detection accuracies.

Figure 16 shows the Precision-Recall and ROC curves for Loy and Eklundh [25] and the Proposed Method #1. Loy and Eklundh [25] fix the maximum number of rotation symmetry centers to be detected (T_1). In Figure 16 (a) and (c), we show the Precision-Recall and ROC curves of [25] and proposed method #1 on rotation symmetry center detection. For comparison, we use the same T_1 as in [25] for the proposed algorithm. Figure 16 (b) and (d) show the Precision-Recall and ROC curves with respect to the threshold for rotation symmetry strength (T_2) in the rotation center decision step. It corresponds to the β in our Proposed Method that sets the threshold for the peak visiting of our two proposed maps (RSS and SSD) (see Section 3.2.1). In rotation symmetry center detection problems, true negative means all pixel points of an image except the true positive rotation centers.

TABLE 1
Quantitative Experimental Results for Level-1 Symmetry (Global: among Objects)

Method	Data Set	TP Center Rate	FP Center Rate	# of Folds	$\mathbf{C_n/D_n/O(2)}$
Loy and Eklundh [25] ECCV2006	13 images with 34 GT	3/34=9%	5/34=15%	2/3=67%	N/A
Lee et.al. [28] CVPR2008	13 images with 34 GT	26/34=76%	4/34=12%	24/26=92%	26/26=100%
Proposed Method #1 (RSS+SSD)	13 images with 34 GT	28/34=82%	4/34=12%	25/28=89%	28/28=100%
Proposed Method #2 (RSS+SSD+LF)	13 images with 34 GT	28/34=82%	8/34=24%	25/28=89%	28/28=100%

TABLE 2
Quantitative Experimental Results for Level-2 Symmetry (on an Object)

Method	Data Set	TP Center Rate	FP Center Rate	# of Folds	$\mathbf{C_n/D_n/O(2)}$
Loy and Eklundh [25] ECCV2006	Synthetic (29 images/48 GT)	31/48=65%	4/48=8%	22/49=45%	N/A
	Real-Single (58 images/58 GT)	50/58=86%	41/58=71%	16/64=25%	N/A
	Real-Multi (21 images/78 GT)	32/78=41%	6/78=8%	12/42=29%	N/A
	Overall (108 images/184 GT)	113/184=61%	51/184=28%	50/155=32%	N/A
Lee et.al. [28] CVPR2008	Synthetic (29 images/48 GT)	36/48=75%	0/48=0%	42/54=78%	44/54=81%
	Real-Single (58 images/58 GT)	25/58=43%	33/58=57%	22/32=69%	24/32=75%
	Real-Multi (21 images/78 GT)	19/78=24%	21/78=27%	18/25=72%	19/25=76%
	Overall (108 images/184 GT)	80/184=43%	54/184=29%	82/111=74%	87/111=78%
Proposed Method #1 (RSS+SSD)	Synthetic (29 images/48 GT)	43/48=90%	12/48=25%	44/62=71%	51/62=82%
	Real-Single (58 images/58 GT)	47/58=81%	37/58=64%	30/59=51%	49/59=83%
	Real-Multi (21 images/78 GT)	52/78=67%	22/78=28%	37/67=55%	50/67=75%
	Overall (108 images/184 GT)	142/184=77%	71/184=39%	111/188=59%	150/188=80%
Proposed Method #2 (RSS+SSD+LF)	Synthetic (29 images/48 GT)	43/48=90%	12/48=25%	44/62=71%	51/62=82%
	Real-Single (58 images/58 GT)	54/58=93%	31/58=53%	35/66=53%	54/66=82%
	Real-Multi (21 images/78 GT)	55/78=71%	22/78=28%	40/70=57%	53/70=76%
	Overall (108 images/184 GT)	152/184=83%	65/184=35%	119/198=60%	158/198=80%

TABLE 3
Quantitative Experimental Results for Level-3 Symmetry(Local: within an Object)

Method	Data Set	TP Center Rate	FP Center Rate	# of Folds	$\mathbf{C_n/D_n/O(2)}$
Loy and Eklundh [25] ECCV2006	7 images with 37 GT	0/37=0%	0/37=0%	N/A	N/A
Lee et.al. [28] CVPR2008	7 images with 37 GT	14/37=38%	0/37=0%	14/14=100%	14/14=100%
Proposed Method #1 (RSS+SSD)	7 images with 37 GT	25/37=68%	0/37=0%	25/25=100%	25/25=100%
Proposed Method #2 (RSS+SSD+LF)	7 images with 37 GT	25/37=68%	0/37=0%	25/25=100%	25/25=100%

TP, FP and GT represent 'True Positive', 'False Positive' and 'Ground Truth' for rotation center detection respectively.
TP Center Rate = # of TP Rotation Centers / # of GT Rotation Centers, FP Center Rate = # of FP Rotation Centers / # of GT Rotation Centers
# of Folds Rate = # of Correct Order of The Rotation Symmetry Group Found / # of Distinct Symmetry Groups of TP Centers
$C_n/D_n/O(2)$ Rate = # of Correct $C_n/D_n/O(2)$ Found / # of Distinct Symmetry Groups of TP Centers
$C_n/D_n/O(2)$ are the cyclic, dihedral and continuous rotation symmetry group types.
Note # of distinct symmetry groups of TP centers $\geq$ # of TP centers, because multiple rotation symmetry groups in an image may share the same rotation center. The complete set of the output images can be found in our supplemental material.

To make ROC curves visible, we set the fixed number (=TP+FP) for true negatives. ROC curves show that for a fixed FP rate, the proposed algorithm has a higher TP rate than the Loy and Eklundh [25] algorithm. In Figure 16 (b), the Loy and Eklundh algorithm shows higher precision when recall<60% but lower precision than the proposed method for higher recall. This indicates the incompleteness of their algorithm for handling all symmetry images in the test set.

4.2 Failure Cases

Though the overall success rates of the proposed method #2 are significantly better than existing rotation symmetry detection algorithms [25] [28] (Tables 1-4), the current detection accuracy on all fronts (rotation center, the order and the type of the symmetry group) is barely satisfactory (e.g. Table 2: 83% or less at the object-level). Figure 17 demonstrates why the correct estimation of the order of the rotation symmetry group can be very challenging. For example: (1) a see-through rotation symmetry supporting region has a rather cluttered background (R81 in Figure 17), and (2) distortion of the rotationally symmetric object can be beyond affine (R105 in Figure 17).

4.3 Algorithm Complexity

Given an image of size IxI, RSS(Section 3.2.1) investigates the linearly sub-sampled points of the image (O(I^2)) and FE is performed at each point to the maximum diameter possible within the image (O(I^1)). Thus, the complexity of the RSS map construction is O(I^3). SSD(Section 3.2.3) also investigates each sampled point of the image, followed by the FE and DFT for phase analysis (O(I^3)). Affine detection and frequency detection perform selectively on the high potential centers. Therefore, the total complexity of the proposed algorithm is O(I^3). The size of a symmetry group (# of folds) does not affect the proposed algorithm complexity. The average processing

TABLE 4
Statistical Significance for The Rotation Center Detection Accuracy Improvements

	Loy and Eklundh [25] → Proposed Method #1			Loy and Eklundh [25] → Proposed Method #2		
	TP	FP	Overall*	TP	FP	Overall*
Level-1	(3→28)	(5→4)	(-2→24)	(3→28)	(5→8)	(-2→20)
P-value	**4.76e-11**	0.3246	**1.50e-08**	**4.76e-11**	0.0831	**1.00e-05**
Level-2	(113→142)	(51→71)	(62→71)	(113→152)	(51→65)	(62→87)
P-value	**2.21e-08**	**4.59e-06**	0.1990	**4.30e-11**	**1.44e-04**	**5.50e-04**
Level-3	(0→25)	(0→0)	(0→25)	(0→25)	(0→0)	(0→25)
P-value	**2.50e-10**	N/A	**4.56e-08**	**2.50e-10**	N/A	**4.56e-08**
All levels	(116→195)	(56→75)	(60→120)	(116→205)	(56→73)	(60→132)
P-value	**3.16e-22**	**2.60e-05**	**1.05e-09**	**1.77e-25**	**5.36e-06**	**8.09e-13**

Level-1 (13 images/ 34 GT), Level-2 (108 images/ 184 GT) and Level-3 (7 images/ 37 GTs). We compute the significance of detection accuracy improvement on each same image with each pair of algorithms. Therefore the paired t-test is used to calculate the p-values. * $Overall_{1\rightarrow 2} = (TP_1 - FP_1) \rightarrow (TP_2 - FP_2)$

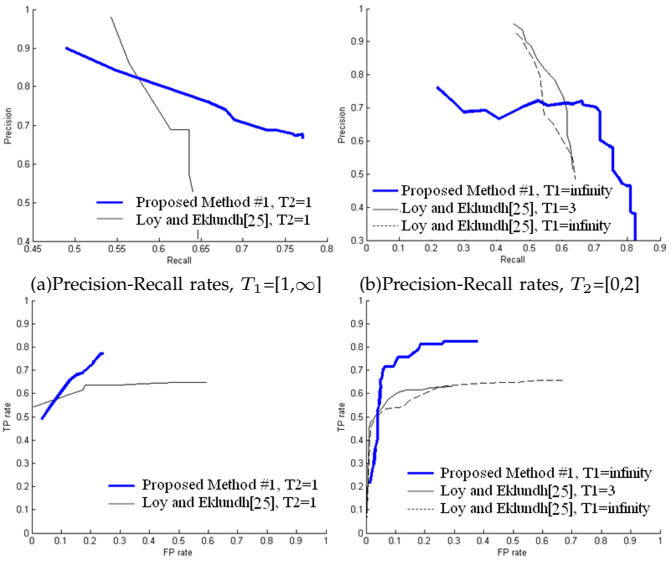

(a)Precision-Recall rates, T_1=[1,∞] (b)Precision-Recall rates, T_2=[0,2]

(c)ROC curves, T_1=[1,∞] (d)ROC curves, T_2=[0, 2]

Fig. 16. Precision-Recall and ROC on object level (level-2) data set: $Precision = \frac{TP}{TP+FP}$, $Recall = \frac{TP}{TP+FN}$, $TPrate = \frac{TP}{TP+FN}$, $FPrate = \frac{FP}{FP+TN}$,where TP = # of true positives, FP = # of false positives, FN = # of false negatives and TN = # of true negatives. T_1 is the allowed maximum number of rotation symmetry centers varying from 1 to ∞. T_2 is the threshold for rotation symmetry strength in the saliency maps varying from 0 to 2. * T_1=3 in (b) & (d) is the default value of the Loy and Eklundh [25] code. ROC curves show that the proposed algorithm outperforms Loy and Eklundh [25] algorithm on rotation center detection, when TP rate > 60%.

time for a 500x500 image is around 50 CPU seconds (coded with Matlab and run on a Windows XP, 3.2GHz Pentium CPU) and the average processing time of the local feature based method [25] is around 8 seconds.

5 Discussion

5.1 The Equivalence of Discrete Fourier Transform and Autocorrelation

Though frequency analysis on the spectral density seems to be a natural choice for finding repeated patterns in an

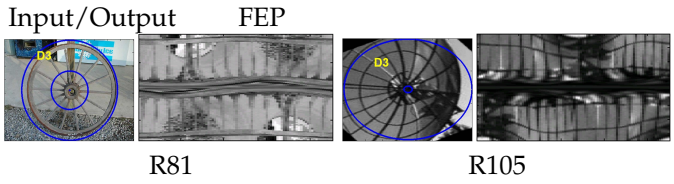

R81 R105

Fig. 17. FEPs of # of folds detection failure cases: R81 and R105. R81: A see-through object: background clutter weakens the foreground rotation symmetry. R105: Non planar curved surface of the object can not be rectified by an affine transformation.

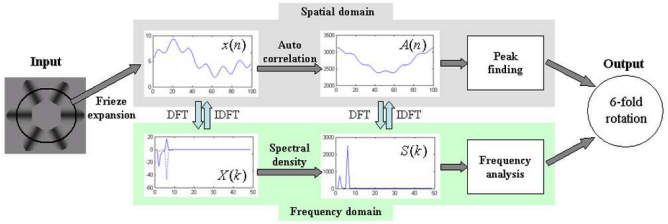

Fig. 18. Relation between spectral density S(k) and autocorrelation A(n). ((a)-(d)-(e)-(f)) is the processes of our algorithm, which is equivalent to using the DFT of autocorrelation ((a)-(b)-(e)-(f)). Peak finding algorithms [7] use (a)-(d)-(e)-(b)-(c) to reduce the time complexity. * DC coefficients are not shown.

image, given only a small number of cycles in a real image, some earlier symmetry detection algorithms choose a peak finding method on the auto-correlation map of input images [26], [34], [40]. For example, [34] used auto-correlation to find the underlying lattice (translation symmetry) in frieze and wallpaper patterns via inverse FFT of the spectral density (for computational efficiency). Based on Wiener-Khinchin theorem [39], we can establish an equivalence relation between the spectral density S(k) and the auto-correlation A(n) for the same input as follows (Figure 18):

$$A(n) = \sum_{m=0}^{N-1} \overline{x(m)} x(n+m) = \sum_{k=1}^{N} S(k) e^{i\frac{2\pi}{N}n(k-1)} \quad (9)$$

From equation (9) one can verify that autocorrelation and spectral density represent the same information in different domains. DFT decomposes autocorrelation into a set of frequency components with the highest coefficient assigned to the strongest component. Our proposed frequency analysis method on the spectral density investigates regularity of autocorrelation by correlating with densely defined components (sine and cosine waves) rather than detecting coarse peak locations in the spatial domain.

5.2 Challenges in Quantitative Evaluations

Our initial exploration of an effective skewed rotation symmetry group detection algorithm has led to some encouraging results (Tables 1-4, Figures 12, 13 and 15). There are several lessons we have learned through this study.

Fig. 19. Various types of ambiguities during groundtruth labeling: (1) types of symmetry groups (cyclic vs dihedral) – R62; (2) # of folds – R95 (from Caltech-256 [37]), R147; (3) affine deformation from a single view is inherently ambiguous: R42.

5.2.1 Ground Truth Labeling

Mathematically, the concept of symmetry group and its associated properties are well-defined [13]; computationally, however, real world symmetry is a discretely sampled *continuous* measure [18]. This imposes tremendous difficulty when it comes to the labeling of the rotation symmetry ground truth on a real image for a quantitative evaluation of the symmetry detection algorithm. For example, to assess three semantic levels of symmetries (level-1: among objects, level-2: on the object, and level-3: on a subpart of an object as shown in Figure 14) can be ambiguous if each rater has a different opinion of what is an "object". In our evaluation step, much thought has been put into constructing a test image set that is sufficiently challenging to all detection algorithms, yet contains apparent symmetries to all human viewers. We resolve this by reaching a consensus among five different human observers and removing any controversial images from the current test image set. The inherent ambiguity in human perception, especially for arbitrary real world scenes, is a research topic in its own right and is beyond the scope of our current paper.

Besides difficulties in labeling the centers of a rotation symmetry, deciding the proper order and the type of a rotation symmetry group can also be challenging for images like the ones shown in Figure 19, even though the rotation symmetry centers are obvious. We have removed such images from our current quantitative evaluation set of symmetry group detection algorithms.

5.2.2 Controlled Variations

Even though we have obtained quantitative evaluation results (Tables 1-4), questions remain on how the rotation symmetry detection algorithms work under variation of imaging conditions. For example, how do the resolution, lighting and perspective distortions of digital images affect the output of the algorithm, and how do the algorithms perform on images with no human-perceived-symmetries? An extensive, detailed and controlled set of tests should be carried out in future research with fine tuned variations of input images (real and synthetic data), perhaps in combination with an investigation of human perception of real world symmetries.

6 Conclusion

We propose a novel skewed rotation symmetry detection algorithm from unsegmented real images with single and multiple rotation symmetry groups. Our method is complete in two senses: first, it detects all types of 2D rotation symmetry groups (cyclic, dihedral and continuous); second, it detects all five properties of a skewed rotation symmetry group (center of rotation, affine deformation, type and number of folds of the symmetry group, and supporting region). The novelty of the proposed approach resides in a clear understanding and exploitation of the interplay between (1) the rotation symmetry groups in Cartesian coordinates and the frieze translation symmetry groups in polar coordinates; and (2) the spatial signal and its frequency (including phase) counterpart. In addition, we also propose and utilize three complementary saliency maps using a representation of global rotation symmetry strength (RSS), symmetrical shape density (SSD) and local feature matching method (LF). Quantitative evaluation and comparison of the proposed method and state of the art algorithms [25], [28] on a test set of 170 images supports the claim that the newly proposed approach achieves statistically significant superior performance (Table 4).

This work is only the first step towards a systematic exploration for computational means to capture various types of real world symmetry. Though the results are encouraging, many research problems remain. We would like to further enhance the complexity ($O(I^3)$) of the current algorithm, improve its robustness on rotation symmetry group center, fold and type detection, and better understand the complex relation between machine and human perceptions of real world symmetries.

Acknowledgments

We thank Loy and Eklundh [25] for their source code for rotation symmetry detection, and Robert Collins and David Capel for helpful discussions. We also thank our associate editor and three reviewers for their constructive comments.

References

[1] P. Locher and C. Nodine, "Symmetry catches the eye," *Eye Movements: from Physiology to Cognition, O'Regan, J. and Levy-Schoen, A., Elsevier Science Publishers B.V.*, 1987.

[2] G. Kootstra, A. Nederveen, and B. de Boer, "Paying attention to symmetry," *Proceedings of the British Machine Vision Conference (BMVC2008)*, pp. 1115–1125, September 2008.

[3] G. Heidemann, "Focus-of-attention from local color symmetries," *IEEE Trans. Pattern Anal. Mach. Intell.*, vol. 26, no. 7, pp. 817–830, 2004.

[4] D. Reisfeld, H. Wolfson, and Y. Yeshurun, "Context free attentional operators: The generalized symmetry transform," *International Journal of Computer Vision*, vol. 14, pp. 119–130, 1995.

[5] I. Kurki and J. Saarinen, "Shape perception in human vision: specialized detectors for concentric spatial structures?" *Neuroscience Letter*, vol. 360, pp. 100–102, 2004.

[6] M. Giurfa, B. Eichmann, and R. Menzel, "Symmetry perception in an insect," *Nature 382*, pp. 458–461, 1996.

[7] M. Park, S. Lee, P.-C. Chen, S. Kashyap, A. A. Butt, and Y. Liu, "Performance evaluation of state-of-the-art discrete symmetry detection algorithms," in *Proceedings of IEEE International Conference on Computer Vision and Pattern Recognition*, June 2008, pp. 1–8.
[8] M. Enquist and A. Arak, "Symmetry, beauty and evolution," *Nature*, vol. 372, pp. 169–172, 1994.
[9] Y. Liu, T. Belkina, J. Hays, and R. Lublinerman, "Image defencing," in *Proceedings of CVPR 2008*, June 2008.
[10] T. Korah and C. Rasmussen, "Analysis of building textures for reconstructing partially occluded facades," in *ECCV08*, 2008, pp. I: 359–372.
[11] M. Pauly, N. J. Mitra, J. Wallner, H. Pottmann, and L. Guibas, "Discovering structural regularity in 3D geometry," *ACM Transactions on Graphics*, vol. 27, no. 3, pp. #43, 1–11, 2008.
[12] Y. Liu, W.-C. Lin, and J. H. Hays, "Near regular texture analysis and manipulation," in *ACM SIGGRAPH 2004*, vol. 23, June 2004, pp. 368–376.
[13] H. Weyl, "Symmetry," *Princeton University Press, ISBN 0-691-02374-3*, 1952.
[14] P. Flynn, "3-d object recognition with symmetric models: Symmetry extraction and encoding," *IEEE Transactions on Pattern Analysis and Machine Intelligence*, vol. 16, no. 8, pp. 814–818, 1994.
[15] S. Lee, Y. Liu, and R. Collins, "Shape variation-based frieze pattern for robust gait recognition," in *Proceedings of CVPR 2007*, June 2007.
[16] T. Riklin-Raviv, N. Kiryati, and N. Sochen, "Segmentation by level sets and symmetry," in *Computer Vision and Pattern Recognition, 2006 IEEE Computer Society Conference on*, June 2006, pp. 1015–1022.
[17] W.-C. Lin and Y. Liu, "A lattice-based mrf model for dynamic near-regular texture tracking," *IEEE Transactions on Pattern Analysis and Machine Intelligence*, vol. 29, no. 1, pp. 777 – 792, May 2007.
[18] H. Zabrodsky, S. Peleg, and D. Avnir, "Symmetry as a continuous feature," *IEEE Transactions on Pattern Analysis and Machine Intelligence*, vol. 17, no. 12, pp. 1154–1166, 1995.
[19] T. Kanade, "Recovery of the three-dimensional shape of an object from a single view," *Artificial Intelligence*, vol. 17, pp. 409–460, 1981.
[20] H. Cornelius, M. Perdoch, J. Matas, and G. Loy, "Efficient symmetry detection using local affine frames," in *Scandinavian Conference on Image Analysis*, 2007, pp. 152–161.
[21] H. Cornelius and G. Loy, "Detecting bilateral symmetry in perspective," in *Computer Vision and Pattern Recognition Workshop*, 2006, p. 191.
[22] L. Van Gool, M. Proesmans, and T. Moons, "Mirror and point symmetry under perspective skewing," in *Proceedings of IEEE International Conference on Computer Vision and Pattern Recognition*, 1996, pp. 285–292.
[23] V. Prasad and L. Davis, "Detecting rotational symmetries," in *Proceedings of IEEE International Conference on Computer Vision*, 2005, pp. 954–961.
[24] Y. Liu, J. Hays, Y. Xu, and H. Shum, "Digital papercutting," in *SIGGRAPH Technical Sketch*, 2005.
[25] G. Loy and J. Eklundh, "Detecting symmetry and symmetric constellations of features," in *European Conference on Computer Vision*, 2006, pp. II: 508–521.
[26] S. Derrode and F. Ghorbel, "Shape analysis and symmetry detection in gray-level objects using the analytical fourier-mellin representation," *Signal Processing*, vol. 84, no. 1, pp. 25–39, 2004.
[27] Y. Keller and Y. Shkolnisky, "A signal processing approach to symmetry detection," *IEEE Transactions on Image Processing*, vol. 15, no. 8, pp. 2198–2207, 2006.
[28] S. Lee, Y. Liu, and R. Collins, "Rotation symmetry group detection via frequency analysis of frieze-expansions," in *Proceedings of IEEE International Conference on Computer Vision and Pattern Recognition*, June 2008, pp. 1–8.
[29] R. Yip, P. Tam, and D. Leung, "A hough transform technique for the detection of rotational symmetry under parallel projection," in *Industrial Electronics, Control and Instrumentation*, 1991, pp. 1259–1263 vol.2.
[30] Y. Lei and K. Wong, "Detection and localisation of reflectional and rotational symmetry under weak perspective projection," *Pattern Recognition*, vol. 32, no. 2, pp. 167–180, 1999.
[31] D. Shen, H. Ip, and E. Teoh, "Robust detection of skewed symmetries," in *International Conference on Pattern Recognition vol.3*, 2000, pp. 1010–1013.
[32] H. Cornelius and G. Loy, "Detecting rotational symmetry under affine projection," in *International Conference on Pattern Recognition*, 2006, pp. II: 292–295.
[33] S. Carlsson, "Symmetry in perspective," in *European Conference on Computer Vision vol.1*, 1998, pp. 249–263.
[34] Y. Liu, R. Collins, and Y. Tsin, "A computational model for periodic pattern perception based on frieze and wallpaper groups," *IEEE Transactions on Pattern Analysis and Machine Intelligence*, vol. 26, no. 3, pp. 354–371, 2004.
[35] R. E. W. Rafael C. Gonzalez, "Digital image processing." *2nd Edition, ISBN 0-20-118075-8.*, 2002.
[36] L. Itti, C. Koch, and E. Niebur, "A model of saliency-based visual attention for rapid scene analysis," *IEEE Transactions on Pattern Analysis and Machine Intelligence*, vol. 20, no. 11, pp. 1254–1259, Nov 1998.
[37] G. Griffin, A. Holub, and P. Perona, "Caltech-256 object category dataset, california institute of technology," *Technical Report 7694*, 2007.
[38] M. Everingham, L. V. Gool, C. K. I. Williams, J. Winn, and A. Zisserman, "The pascal visual object classes challenge 2007 results," *http://www.pascalnetwork.org/challenges/VOC/voc2007/workshop/index.html*.
[39] J. G. Proakis and D. G. Manolakis, "Digital signal processing. principles, algorithms, and applications." *Third Edition. ISBN 0-13-373762-4.*, 1996.
[40] H.-C. Lin, L.-L. Wang, and S.-N. Yang, "Extracting periodicity of a regular texture based on autocorrelation functions," *Pattern Recogn. Lett.*, vol. 18, no. 5, pp. 433–443, 1997.

Seungkyu Lee received the BS and MS degrees in electrical engineering from Korea Advanced Institute of Science and Technology, Daejeon, South Korea, in 1997 and 1999, respectively, and MSc in electrical engineering from The Pennsylvania State University in 2007. He is currently working toward the PhD degree in the Department of Computer Science and Engineering at The Pennsylvania State University - University Park. His current research interests include symmetry feature detection, human body motion recognition and object recognition. He is a student member of the IEEE and the IEEE Computer Society.

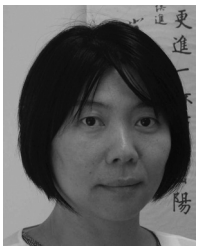

Yanxi Liu received the BS degree in physics/electrical engineering from Beijing, China, the PhD degree in computer science for group theory applications in robotics from the University of Massachusetts, Amherst, and postdoctoral training at LIFIA/IMAG, Grenoble, France. She also spent one year at the US National Science Foundation (NSF) Center for Discrete Mathematics and Theoretical Computer Science (DIMACS) with an NSF Research Education Fellowship Award. She was an associate research professor in the Robotics Institute of Carnegie Mellon University before she joined the Computer Science Engineering and Electrical Engineering Departments of The Pennsylvania State University in the fall of 2006 as a tenured faculty member and the codirector of the Lab for Perception, Action, and Cognition (LPAC). Her research interests span a wide range of applications, including computer vision, computer graphics, robotics, human perception, and computer-aided diagnosis in medicine, with a theme on computational symmetry/regularity and discriminative subspace learning. She chaired the First International Workshop on Computer Vision for Biomedical Image Applications (CVBIA) in Beijing and coedited the book CVBIA: Current Techniques and Future Trends (Springer-Verlag LNCS). She served as a multiyear chartered study section member for the US National Institutes of Health (biomedical computing and health informatics) and recently served as an area chair/organizing committee member for CVPR 08/MICCAI 08/CVPR 09. She is a senior member of the IEEE and the IEEE Computer Society.